GEOPHYSICS

Surface deformation associated with fractures near the 2019 Ridgecrest earthquake sequence

Xiaohua Xu[1]*, David T. Sandwell[1], Lauren A. Ward[2], Chris W. D. Milliner[3], Bridget R. Smith-Konter[2], Peng Fang[1], Yehuda Bock[1]

Contemporary earthquake hazard models hinge on an understanding of how strain is distributed in the crust and the ability to precisely detect millimeter-scale deformation over broad regions of active faulting. Satellite radar observations revealed hundreds of previously unmapped linear strain concentrations (or fractures) surrounding the 2019 Ridgecrest earthquake sequence. We documented and analyzed displacements and widths of 169 of these fractures. Although most fractures are displaced in the direction of the prevailing tectonic stress (prograde), a large number of them are displaced in the opposite (retrograde) direction. We developed a model to explain the existence and behavior of these displacements. A major implication is that much of the prograde tectonic strain is accommodated by frictional slip on many preexisting faults.

On 4 to 5 July 2019, the moment magnitude (M_w) 6.4 and M_w 7.1 Ridgecrest earthquake sequence ruptured a geometrically complex system of conjugate faults within the Walker Lane belt to the north of the eastern California shear zone (ECSZ), 17 km northeast of the city of Ridgecrest, California (*1*). Field scientists reported more than 5 m of dextral slip near the epicenter of the NW-SE M_w 7.1 rupture and 1 to 2 m of sinistral slip along the NE-SW M_w 6.4 rupture, whereas observations of distributed slip went largely undetected in rapid-response field surveys (*2*). Crustal deformation from the Ridgecrest earthquake sequence, however, was extremely well imaged by the twin Sentinel-1 radar satellites, providing an opportunity to examine high-resolution slip behavior of hundreds of very small crustal fractures in near real time. Not only did these distinctive remote-sensing observations aid early ground survey efforts, they also provide insight into candidate mechanisms of strain concentrations nearby the main rupture. Here, we investigate compelling evidence of discrete and distributed, yet contrasting, stress-induced surface fractures from two physically distinct deformation processes surrounding the Ridgecrest earthquake sequence: frictional sliding on preexisting faults and elastic deformation of compliant fault zones. These fractures are largely invisible to ground surveys and are only associated with infrequent major earthquakes.

Previous studies have documented small amounts of surface displacement on mapped faults nearby major large earthquakes (*3*–*8*). Most of the triggered faults slip in the direction of the prevailing tectonic stress (prograde). This slip could be driven by dynamic stresses from elastic wave propagation or by permanent Coulomb stress changes. However, in a small number of cases associated with the 1992 Landers and 1999 Hector Mine earthquakes, the polarity (sense of offset across the fault) of the displacement was opposite to the prevailing stress (retrograde) (*9*–*11*). If these features represented true retrograde fault slip, the observations may imply that the relatively small stress release from the earthquake exceeded the tectonic stress, representative of a frictional slip model. An alternate explanation is that the retrograde displacement is due to strain localization on a compliant fault zone (*10*). If faults exhibit a relatively wide damage zone of low shear modulus (*12*), then the elastic strain will be concentrated in the damage zone and have a polarity that matches the Coulomb stress change (*10*, *11*). This compliant fault zone model requires a preexisting fault that was damaged by historic ruptures.

The Sentinel-1 (*14*) and Advanced Land Observing Satellite-2 (ALOS-2) (*15*) satellites acquired high coherence interferograms that span the two Ridgecrest events. We generated phase gradient maps (Fig. 1A) (*13*, *16*) [(*17*) and table S1] from stacks of the C-band Sentinel-1 data to identify 291 surface fractures. We then constructed east-west and up-down/south-north deformation maps from the difference and sum of stacked ascending and descending line-of-sight (LOS) displacement maps (*17*). We used these to measure the polarity and width of the lineaments' deformations. The polarities of 109 of the deformations are consistent with the prevailing tectonic stress (*18*), although 60 have well-resolved retrograde displacements (Fig. 1B). We could not classify 122 of the fractures.

To interpret these displacements, we developed a Coulomb stress forward model from a detailed earthquake rupture model. We constructed the rupture model from an inversion of a compilation of geodetic data (*19*) [(*17*) and figs. S2 and S3]. Measurements of surface motion are provided by LOS displacements from two look directions of both the Sentinel-1A and -1B and ALOS-2 satellites and along-track interferometry from the ALOS-2 satellite. Global Navigation Satellite System (GNSS) offsets from 92 stations were used to constrain the large-scale deformation (*20*), where the GNSS product, which captured surface motion between the times of the two events, enabled a partial decomposition of the two ruptures, suggesting that there was substantial slip on both faults from each event. We constrained near-fault deformation in areas of possible interferometric synthetic aperture radar (InSAR) decorrelation with offsets estimated from Sentinel-2 imagery (*21*). Our slip model reveals a shallow slip deficit (SSD) (*22*) of 29%, which is larger than any recent major strike-slip earthquake in the ECSZ and Baja California (*19*) (i.e., 18% for Landers, 3% for Hector Mine, and 11% for El-Mayor Cucapah). This larger SSD might indicate the existence of a much thicker sedimentary layer or distributed shallow faulting over this region.

Using our slip model, we calculated tensor stress change at the surface of the Earth (*23*) [shear modulus (G) of 10 GPa] and projected it onto vertical planes parallel to each of the fracture segments to compute Coulomb stress change (fig. S4). We did this for a range of frictional coefficients (0.01 to 0.99) and background stress amplitudes (0.01 to 1 MPa). We assumed the regional tectonic deviatoric stress to be north-south compression and equal east-west extension (*18*). The polarity of the fracture displacements we observed (Fig. 1) was compared with the combined earthquake and regional deviatoric tectonic stress to achieve the best agreement (number matching to total). We found that the best agreement was a relatively small additional deviatoric tectonic stress of 0.4 MPa (fig. S4, bottom) and a low frictional coefficient (0.1). The transition in displacement polarity from prograde to retrograde is quite sensitive to the amplitude of this regional deviatoric tectonic stress. We speculate that this small background stress reflects only a portion of real surface stress and that the stress deeper in the crust is much higher.

Results from our analysis imply that the static stress change from the earthquake controls the polarity of the surface fractures. We then sought to determine if the observed deformation is from true fault slip due to the fault frictional strength being exceeded or an elastic response of a wide compliant fault zone due to the Coulomb stress change (Fig. 2A). The simplest compliant fault zone model has a damage zone with certain width (w) and lower

[1]Institute of Geophysics and Planetary Physics, Scripps Institution of Oceanography, University of California San Diego, La Jolla, CA, USA. [2]Department of Earth Sciences, University of Hawaii at Manoa, Honolulu, HI, USA. [3]Jet Propulsion Laboratory, California Institute of Technology, Pasadena, CA, USA.
*Corresponding author. Email: xix016@ucsd.edu

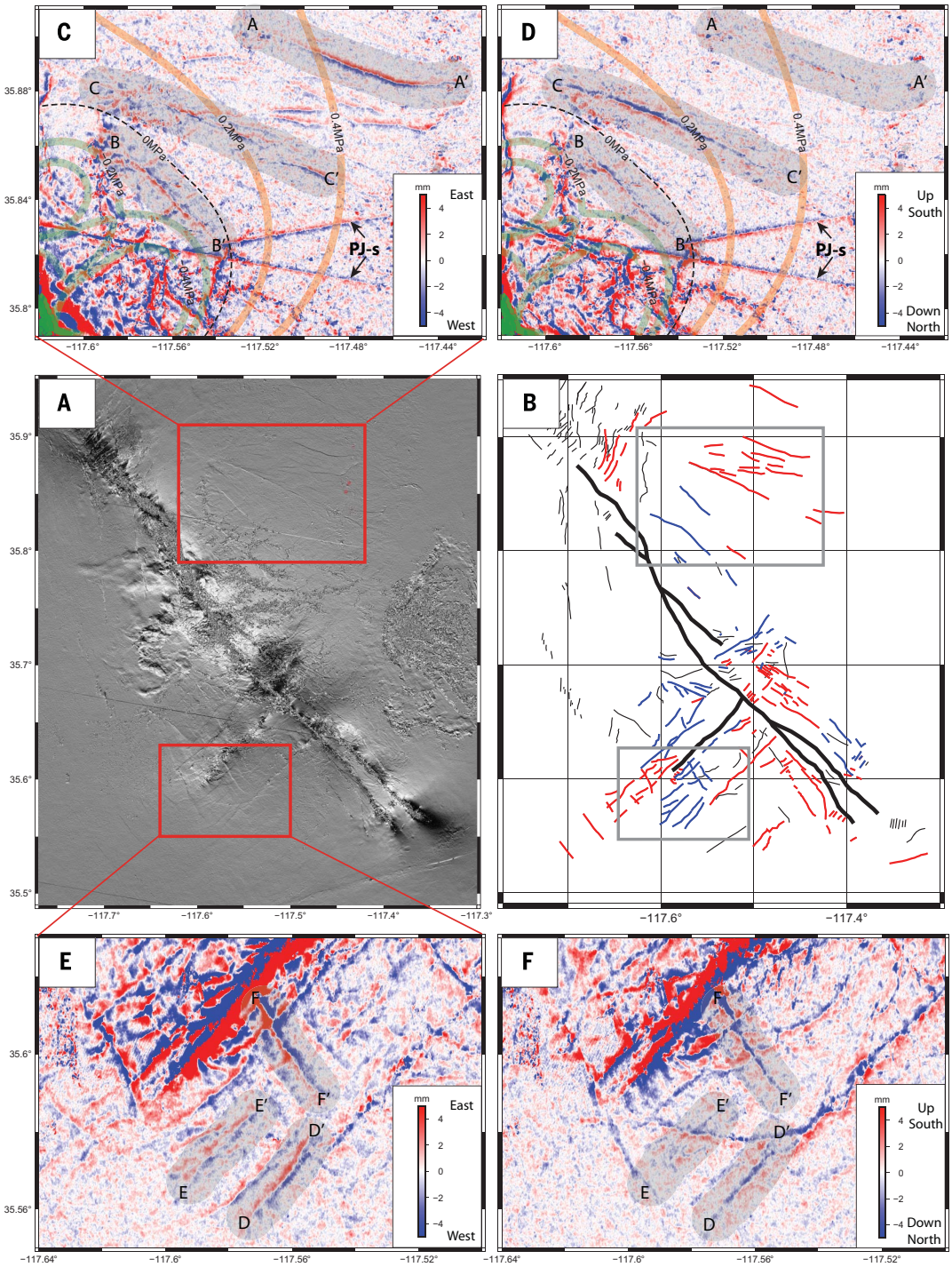

Fig. 1. Observations of fractures nearby the Ridgecrest earthquake sequence revealed by Sentinel-1 radar interferometry. (**A**) Phase gradient map from stacked Sentinel-1 interferograms revealing ~300 surface fractures around the Ridgecrest earthquake sequence region (*13*). (**B**) These fractures have been classified as prograde (red, 109 fractures), retrograde (blue, 60 fractures), and undetermined (black, 122 fractures) based on high-pass filtered (800 m) and decomposed (*13*) LOS deformation maps (upper and lower rows). The regions enclosed by the gray boxes cover exactly the same area as the red boxes in (A). (**C** and **D**) The north quadrant of the M_w 7.1 rupture has both prograde (A-A′) and retrograde (B-B′) fractures that occur in areas of positive (orange contours) and negative (green contours) Coulomb stress, respectively. Coulomb stress is computed with a receiver fault orientation aligned with the M_w 7.1 rupture (44° NW). Profile A-A′ has a prominent right-lateral east-west signature but small up-down/south-north signature. Profile B-B′ has a prominent left-lateral east-west signature as well as a substantial combined left-lateral south-north and/or downward up-down signature. Profile C-C′ is transitional, right-lateral (prograde) at the eastern end and mainly up-down at the western end with slight right-lateral motion. (**E** and **F**) The south quadrant near the M_w 6.4 rupture has several right-lateral (retrograde) fractures (D-D′ and E-E′) as well as left-lateral (retrograde) fractures (F-F′). Both sets are in an area of negative Coulomb stress based on the respective fault orientations. Many of the fractures (D-D′ and F-F′) have prominent downward vertical signatures resulting from extensional stress. Note that the very straight lines in decomposed maps (C) and (D), which are marked by bold "PJ-s" and arrows, are not real fractures but radar phase jumps (PJ-s) across burst boundaries caused by the design of the Sentinel-1 radar and misregistration owing to azimuthal deformation from the earthquake.

shear modulus (G_l), embedded in a half space of higher shear modulus (G_h) (Fig. 2A). When a shear stress change ($\Delta\sigma_t$) is applied, a strain localization in the compliant zone appears as a step in the deformation profile (D) across the fault. From these parameters, we can estimate the ratio of the shear modulus in the fault zone to the surrounding shear modulus (*10*, *24*):

$$\frac{G_l}{G_h} = \frac{1}{\frac{DG_h}{w\Delta\sigma_t} + 1} \quad (1)$$

A shear modulus ratio of less than about 0.3 is physically difficult to explain (*25*), whereas a very small contrast is equivalent to a very strong strain concentration, consistent with true fault slip. Compliant elastic strain is thus possible for larger modulus ratios.

We measured the amplitude and width of deformation for many profiles crossing each

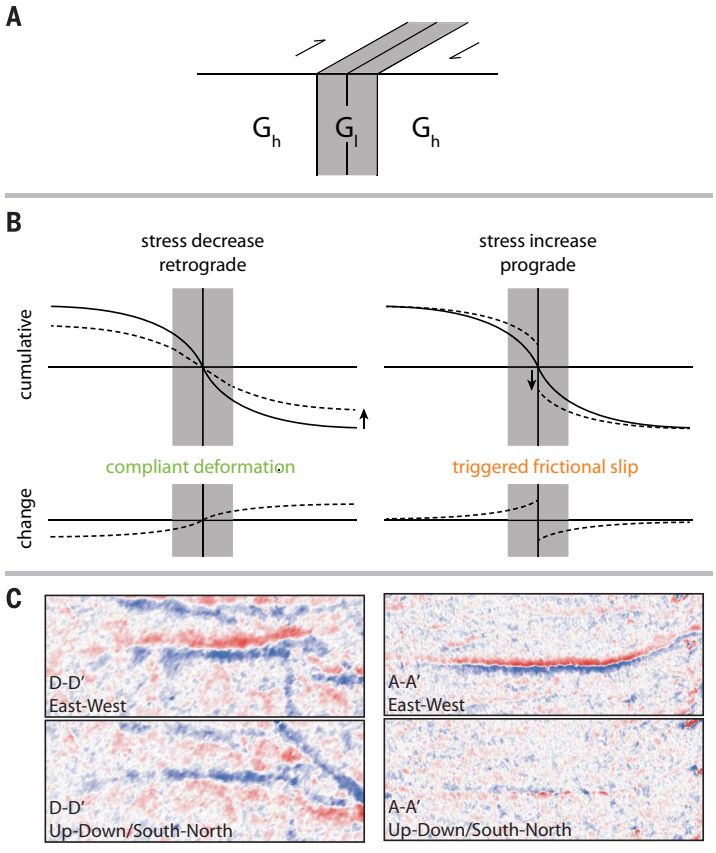

Fig. 2. Response of a critically stressed fault zone to a change in stress from a nearby large earthquake. (**A**) Schematic of a fault surrounded by a compliant zone of relatively low-shear modulus G_l in a half-space of normal shear modulus G_h. (**B**) A stress change ($\Delta\sigma_t$) from a major nearby earthquake produces two types of surface deformation. Solid lines represent across-fault displacement profiles for the elastic half-space model shown in (A). Dashed lines represent the displacement behavior for a compliant zone subject to a stress increase or decrease. (Left) A stress decrease with respect to the prevailing tectonic stress results in retrograde elastic deformation in the compliant zone. (Right) A stress increase will produce prograde deformation. Resulting fractures could thus be elastic deformation over the wide compliant zone or triggered frictional sliding over a narrow fault zone. (**C**) Example InSAR results from Fig. 1 corresponding to the two slip mechanisms illustrated in (B).

fracture (fig. S5) from the east-west deformation maps and projected the displacement onto the orientation of the fault to estimate the shear modulus reduction for each fracture (*17*) (Fig. 3). We found that the amplitudes of the measured prograde and retrograde displacements are similar, between 1 and 30 mm. However, the prograde deformation widths are systematically narrower (~100 m) than the retrograde deformation widths (200 to 500 m). This results in unreasonably small shear modulus ratios (less than 0.3) for the prograde deformations, compared with the shear modulus ratios of between 0.3 and 0.8 for the retrograde deformations. The best spatial resolution from Sentinel-1 Terrain Observation with Progressive Scan (TOPS) data is about 30 m, so prograde deformations are possibly narrower. From this analysis, we propose that the prograde deformations largely represent fault frictional slip, whereas the retrograde deformations are more likely due to elastic response of a compliant fault zone. These widths are much smaller than the ~1- to 2-km compliant fault zone width for retrograde displacements from the Hector Mine earthquake (*10*). Distribution of the measured and calculated parameters with respect to prograde and retrograde fractures present a composition of mechanism with analogy to a "ratchet" system, that is, the fault could deform in both directions, but true fault slip only occurs in the direction of prevailing tectonic stress.

Based on this analysis, we have developed a conceptual model for shallow displacement on faults in response to large ruptures (Fig. 2B and fig. S6). This region to the north of the ECSZ has a very high spatial density of conjugate faults that have slipped in the past in response to the regional tectonic stress (*1*). This interaction between the regional stress and earthquakes has been inferred to result in the faults being critically stressed, very close to failure by frictional sliding. The Ridgecrest earthquakes represent a major failure on two of these faults that subsequently changed the stress in the region. A Coulomb stress increment that is aligned with the preexisting tectonic stress increases the stress on the prograde faults to a state beyond their sliding strength, causing them to deform inelastically as frictional slip, especially at shallow depth where the overburden normal stress is low. A Coulomb stress increment that is opposed to the preexisting tectonic stress lowers the stress on the retrograde faults, moving them away from failure, so they respond elastically over the wide damage zone of relatively low shear modulus. Between times of major earthquakes, the gradual increase in regional tectonic stress will bring the stress level of the retrograde faults closer to the critical level. The prograde faults could undergo aseismic slip or creep to maintain a critical stress level.

We examined two quadrants of the overall stress pattern where there is a transition between the prograde and retrograde faults and the changes in vertical deformation. The first quadrant is the region to the northeast of the epicenter of the M_w 7.1 event (Fig. 1, C and D). The dashed curved line at 0 MPa marks the transition of Coulomb stress along the M_w 7.1 rupture direction. One fault (A-A′) east and north of this zone, where Coulomb stress is positive, has a clear and narrow right-lateral (prograde) deformation (east-west) and no vertical deformation (up-down), in agreement with the frictional slip model. West and south of the transition zone, there is a fault (B-B′) that has a broad left-lateral (retrograde) deformation (east-west) and also a mixture of vertical (up-down) and left-lateral (south-north) deformation. Both deformation components are consistent with compliant zone fault slip behavior (*10*). Between these two faults, there is a fault (C-C′) that has a transition from right-lateral slip and little vertical motion on the eastern end to slight right-lateral offset and prominent downward vertical motion on the western end inside the 0.2-MPa Coulomb stress change contour. This fault is a rare case where, with a small increase in Coulomb stress, this fault was able to maintain its continuum and not surpass its critical stress status to produce frictional failure. Retrograde fractures are also prominent south of the M_w 6.4 event (Fig. 1, E and F). There are two sets of retrograde fractures in this area: right-lateral fractures parallel to the M_w 6.4 rupture and left-lateral fractures perpendicular to the M_w 6.4 rupture. Both sets are in areas of negative Coulomb stress change for their respective fault orientations. A number of these faults also have downward vertical signatures related to extensional stress in this quadrant (fig. S1). One would need to develop a three-dimensional compliant fault model to better understand the combined strike-slip and vertical deformations seen in these areas.

We found substantial differences between the compliant fault zones imaged in our analysis and compliant zone images from the 1999 Hector Mine earthquake (*9*, *10*). The typical widths of the deformation for the Roadman and Calico faults in the Hector Mine region were 1 to 2 km, whereas the retrograde deformation zones in the Ridgecrest region were

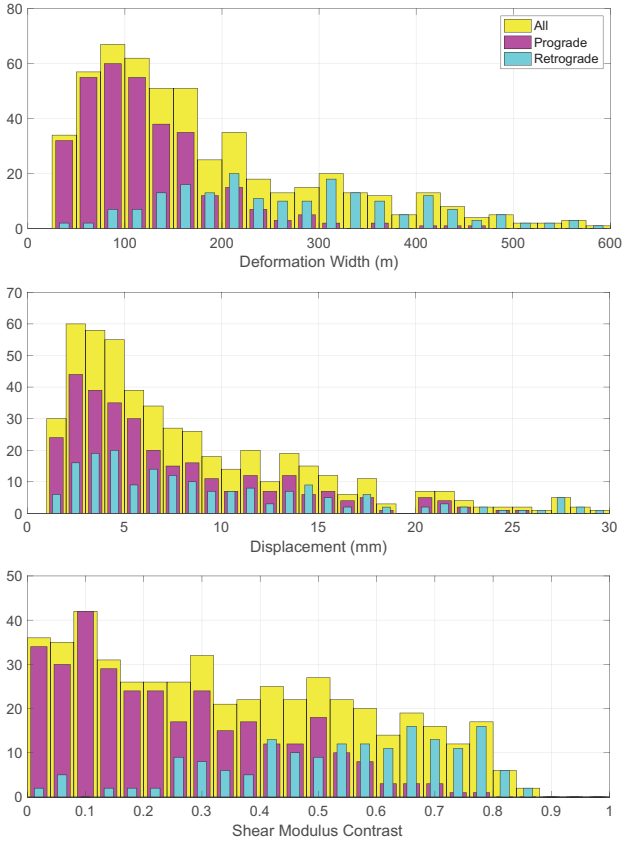

Fig. 3. Histograms of measured and computed parameters for the deformation profiles of the fractures. Show are measured deformation width (top), measured displacement amplitude (middle), and computed shear modulus contrast with Eq. 1 (bottom) for all fractures (yellow), prograde fractures (magenta), and retrograde fractures (cyan).

typically 200 to 500 m wide. Nevertheless, both areas have similar shear modulus reductions of 0.4 to 0.8. These are in agreement with the seismic velocity reduction observed on the San Andreas and San Jacinto faults (*11*). The difference in the widths of the damage zones may reflect the maturity of these faults (*26*), indicating that possible damage zones are well developed even at the faults' young age (*27*). Damage zone widths will increase with time as repeated rupture damage accumulates and becomes "fossilized" (*26*). By contrast, the amplitude of the shear modulus reduction may saturate at ~0.4, which explains the similarities between the two areas. The Rodman and Calico faults are relatively mature, having ~10 km of offset (*28*), whereas the small unnamed faults in the Ridgecrest area probably have much smaller offsets. Now that these faults have been mapped and characterized by Sentinel-1 InSAR, additional geological surveys will help to clarify their overall slip and thus maturity.

Compared with previous studies of deformations nearby large strike-slip earthquakes, the 2019 Ridgecrest earthquake sequence revealed an exceptional number of previously unmapped surface fractures. Whereas the prograde fractures might be new surface cracks that developed during the M_w 7.1 rupture, the retrograde compliant deformation must be associated with preexisting faults. These observations provided in situ records showing that very young and immature faults also have well-developed damage zones, which was previously thought to only occur for mature and repeatedly ruptured faults. Based on our analysis, all large earthquakes likely induce linear strain concentrations on preexisting faults. Stacking and phase gradient analysis of repeated images provides a new tool for discovering these faults, especially for areas with low strain accumulation. Such a large number of fractures were observed for the first time mainly because of the frequent, high-quality observations provided by the Sentinel-1 satellites, combined with the arid environment of the Mojave Desert region. These types of fractures may be ubiquitous to the ECSZ and many other diffuse strike-slip fault systems. Distributed as they are, these structures could account for the larger shallow slip deficit derived from the Ridgecrest earthquake sequence. A major implication of this result is that much of the "off fault" strain in the Mojave shear zone is due to permanent inelastic deformation on many small faults.

REFERENCES AND NOTES

1. Z. E. Ross *et al.*, *Science* **366**, 346–351 (2019).
2. D. J. Ponti *et al.*, *Seismol. Res. Lett.* **91**, 2942–2959 (2020).
3. P. L. Williams, S. F. McGill, K. E. Sieh, C. R. Allen, J. N. Louie, *Bull. Seismol. Soc. Am.* **78**, 1112–1122 (1988).
4. P. Bodin, R. Bilham, J. Behr, J. Gomberg, K. W. Hudnut, *Bull. Seismol. Soc. Am.* **84**, 806–816 (1994).
5. M. J. Rymer, *Bull. Seismol. Soc. Am.* **90**, 832–848 (2000).
6. T. Wright, E. Fielding, B. Parsons, *Geophys. Res. Lett.* **28**, 1079–1082 (2001).
7. X. Xu *et al.*, *Geophys. Res. Lett.* **45**, 10,259–10,268 (2018).
8. H. Goto, H. Tsutsumi, S. Toda, Y. Kumahara, *Earth Planets Space* **69**, 26 (2017).
9. D. T. Sandwell, L. Sichoix, D. Agnew, Y. Bock, J. B. Minster, *Geophys. Res. Lett.* **27**, 3101–3104 (2000).
10. Y. Fialko *et al.*, *Science* **297**, 1858–1862 (2002).
11. Y. Fialko, *J. Geophys. Res. Solid Earth* **109**, B03307 (2004).
12. A. A. Allam, Y. Ben-Zion, *Geophys. J. Int.* **190**, 1181–1196 (2012).
13. X. Xu, D. T. Sandwell, B. Smith-Konter, *Seismol. Res. Lett.* **91**, 1979–1985 (2020).
14. R. Torres *et al.*, *Remote Sens. Environ.* **120**, 9–24 (2012).
15. A. Rosenqvist *et al.*, *Remote Sens. Environ.* **155**, 3–12 (2014).
16. D. T. Sandwell, E. J. Price, *J. Geophys. Res. Solid Earth* **103**, 30183–30204 (1998).
17. Materials and methods are available as supplementary materials.
18. J. Townend, M. D. Zoback, *Geophys. Res. Lett.* **31**, L15S11 (2004).
19. X. Xu *et al.*, *Geophys. J. Int.* **204**, 1867–1886 (2016).
20. E. Klein *et al.*, *J. Geophys. Res. Solid Earth* **124**, 12189–12223 (2019).
21. C. Milliner, A. Donnellan, *Seismol. Res. Lett.* **91**, 1986–1997 (2020).
22. Y. Fialko, D. Sandwell, M. Simons, P. Rosen, *Nature* **435**, 295–299 (2005).
23. Y. Okada, *Bull. Seismol. Soc. Am.* **82**, 1018–1040 (1992).
24. P. Segall, *Earthquake and Volcano Deformation* (Princeton Univ. Press, 2010).
25. E. S. Cochran *et al.*, *Geology* **37**, 315–318 (2009).
26. J. F. Dolan, B. D. Haravitch, *Earth Planet. Sci. Lett.* **388**, 38–47 (2014).
27. H. M. Savage, E. E. Brodsky, *J. Geophys. Res. Solid Earth* **116**, B03405 (2011).
28. M. Oskin, L. Perg, D. Blumentritt, S. Mukhopadhyay, A. Iriondo, *J. Geophys. Res. Solid Earth* **112**, B03402 (2007).

ACKNOWLEDGMENTS

We thank T. Wright, K. Scharer, and an anonymous reviewer for their valuable suggestions and comments that strengthened this manuscript. **Funding:** This study was funded by the NASA Earth Surface and Interior Program (80NSSC19K1043), NASA Making Earth System Data Records for Use in Research Environments program (NNH17ZDA001N-MEASURES), the National Science Foundation (OAC-1834807 and EAR-1614875), and the Southern California Earthquake Center (SCEC) (19083). SCEC is funded by the NSF cooperative agreement EAR-1033462 and USGS cooperative agreement G12AC20038. **Author contributions:** X.X. analyzed InSAR images, performed source inversion and Coulomb stress analysis, computed the polarity and stress matching, performed profile analysis, calculated the histogram of parameters, worked on the conceptual model, and wrote the manuscript; D.T.S. analyzed InSAR images, performed profile analysis, worked on the conceptual model, and wrote the manuscript; L.A.W. initialized the Coulomb stress analysis and edited the manuscript; C.W.D.M. provided the optical imagery data to constrain the source model and edited the manuscript; B.R.S.-K. initialized the Coulomb stress analysis, worked on getting early InSAR acquisitions, and edited the manuscript; and P.F. and Y.B. analyzed and refined the GNSS offsets used in the source inversion. **Competing interests:** All authors declare no conflicts of interests. **Data and materials availability:** The Sentinel-1 images are copyright of the European Space Agency (ESA) and are freely available through the Sentinel-1 data hub, with data and orbital products archived and available at the Alaska Satellite Facility (ASF). The ALOS-2 images are copyright of the Japanese Aerospace and Exploration Agency (JAXA) and are provided under ALOS-2 RA6 research project 3071. GNSS offsets are processed and archived at Scripps Orbit and Permanent Array Center (SOPAC). All processed data are available from the authors on request.

SUPPLEMENTARY MATERIALS

science.sciencemag.org/content/370/6516/605/suppl/DC1
Materials and Methods
Figs. S1 to S6
Table S1
References (*29*–*33*)

4 June 2020; accepted 11 September 2020
10.1126/science.abd1690

Science

Surface deformation associated with fractures near the 2019 Ridgecrest earthquake sequence

Xiaohua Xu, David T. Sandwell, Lauren A. Ward, Chris W. D. Milliner, Bridget R. Smith-Konter, Peng Fang and Yehuda Bock

Science **370** (6516), 605-608.
DOI: 10.1126/science.abd1690

Mapping out backward motion

Most deformation associated with an earthquake is, not surprisingly, in the same direction as the fault rupture. Xu *et al.* used satellite imaging to find areas of deformation associated with the 2019 Ridgecrest earthquake sequence that moved in the opposite direction. These regions moved in this direction because of inelastic deformation, which helped to accommodate the overall fault rupture for the sequence. The observations were possible because of improved radar imaging and are likely more common than previously believed.

Science, this issue p. 605

science.sciencemag.org/content/370/6516/605/suppl/DC1

Supplementary Materials for

Surface deformation associated with fractures near the 2019 Ridgecrest earthquake sequence

Xiaohua Xu*, David T. Sandwell, Lauren A. Ward, Chris W. D. Milliner, Bridget R. Smith-Konter, Peng Fang, Yehuda Bock

*Corresponding author. Email: xix016@ucsd.edu

Published 30 October 2020, *Science* **370**, 605 (2020)
DOI: 10.1126/science.abd1690

This PDF file includes:

Materials and Methods

InSAR processing details

The InSAR data used in this analysis were Terrain Observation with Progressive Scan (TOPS) from Sentinel-1A/B satellites operated by the European Space Agency (*14*) (See Table S1 for pairs of interferograms). The data were processed using an open source InSAR software, GMTSAR (https://github.com/gmtsar/gmtsar). To generate phase-gradient maps, the data were processed at full resolution with a derivative filter (*16*). For this, the gradient operation is performed on the real and imaginary part of the Single-Look-Complex (SLC) images and then combined with the formula below,

$$\nabla\phi(\mathbf{x}) = \frac{R\nabla I - I\nabla R}{R^2 + I^2}$$

where the gradient operator is $\nabla = \left(\frac{\partial}{\partial r}, \frac{\partial}{\partial a}\right)$, with $\boldsymbol{r}$ and $\boldsymbol{a}$ denoting the direction of gradient along-range (look) and azimuth (flight). The numerical derivative filter was designed to avoid aliasing of short wavelength noise to longer wavelengths so a central difference was combined with a 60-m wavelength Gaussian low pass filter (note the TOPS mode has ~13m sampling along track). These phase gradient maps were then stacked to further reduce noise from troposphere and ionosphere effects, phase noise, etc. In addition, the InSAR phase was also used to produced full-resolution interferograms and unwrapped with SNAPHU software (*29*). We stacked phase data within each track, and then decomposed them into East-West (subtraction and then scale) and South-North/Up-Down (addition and then scale) components, taking advantage of the largely symmetric look angles. (Note the average east-E, north-N, up-U look vectors for descending and ascending are [0.633, -0.112, 0.765] and [-0.636, -0.112, 0.763] respectively, so this approximation is excellent.) Last, we filter the decomposed maps using an 800-m Gaussian high-pass filter to reveal the motion of the fractures. This wavelength is chosen as some fractures are close to each other with spacing at ~1 km.

Table S1: Interferometric Pairs vs. Perpendicular Baseline ($B_\perp$)

Direction	Dates	$B_\perp$ (m)
Descending	2019/06/22 – 2019/07/16	87.79
Average Look Vector:	2019/06/22 – 2019/07/28	38.09
[0.633, -0.112, 0.765]	2019/07/04 – 2019/07/16 (Fig1b)	29.68
	2019/07/04 – 2019/07/28	31.15
Ascending	2019/06/28 – 2019/07/10	63.38
Average Look Vector:	2019/06/28 – 2019/07/16	35.98
[-0.636, -0.112, 0.763]	2019/06/28 – 2019/07/22	12.37
	2019/06/28 – 2019/07/28	25.96
	2019/06/28 – 2019/08/03	94.57
	2019/07/04 – 2019/07/10 (Fig1c)	126.64
	2019/07/04 – 2019/07/16	27.26
	2019/07/04 – 2019/07/22	75.62
	2019/07/04 – 2019/07/28	89.20
	2019/07/04 – 2019/08/03	31.32

Kinematic inversion approach

The inversion approach adopted here largely follows (*19*), in which observations from InSAR phase data, along-track interferogram data, GNSS data, and on-fault slip estimate data can be combined into one inversion. The only difference is that we used GNSS data to separate the two events, which is described by the equation bellow, similar to (*30*),

$$\begin{bmatrix} W_pG_p & W_pG_p & W_pW_rR_p \\ W_aG_a & W_aG_a & W_aW_rR_a \\ W_gG_g & 0 & 0 \\ 0 & W_gG_g & 0 \\ W_oG_o & W_oG_o & 0 \\ \lambda S & 0 & 0 \\ 0 & \lambda S & 0 \end{bmatrix} \begin{bmatrix} m_1 \\ m_2 \\ m_r \end{bmatrix} = \begin{bmatrix} W_pd_p \\ W_ad_a \\ W_gd_{g1} \\ W_gd_{g2} \\ W_od_o \\ 0 \\ 0 \end{bmatrix}$$

where G_p, G_a, G_g, G_o are Green's functions matrix components for InSAR LOS displacements (p), along-track displacements (a) , GNSS displacements (g), and fault offset (o) from optical imagery; W_p, W_a, W_g, W_o are weights solved to provide the maximum overall fitting to different dataset; W_r is an extra weight for ramp estimates for each dataset; R_p, R_a are planar ramp functions for each individual dataset from different tracks; d_p, d_a, d_g, d_o are corresponding data vectors, with d_{g1} for the *Mw* 6.4 earthquake and d_{g2} for *Mw* 7.1 earthquake; m_1 and m_2 are solved dislocation slip vectors on the fault plane, and m_r are ramp parameters for each individual dataset. The achieved

fitting for each dataset has a variance reduction of 96%, 87%, 97%, 99% for InSAR phase, along-track interferogram, GNSS data, and on-fault offset estimates from optical imagery, respectively. The solved corresponding moment magnitude for each earthquake is *Mw* 6.44 and *Mw* 7.03, with a 32 GPa assumed average shear modulus.

Coulomb stress, polarity matching and profile analysis

The decomposed E-W and S-N/U-D maps (Figure S1) were used to determine the polarity (prograde or retrograde) of the surface fractures. The sense of motion (left-lateral or right-lateral) was established from the E-W component only. Thus, a few N-S oriented fractures could not be analyzed. Based on the regional tectonic stress (*18*), we also calculated the expected sense of motion; NW-SE oriented faults should be right-lateral and NE-SW oriented faults should be left-lateral. If the sense of motion from the InSAR observations matched the expected motion from tectonic stress, then the fracture was identified as prograde. If the sense of motion from the InSAR observation contradicted the expected, then the fracture was identified as retrograde. All fractures were assumed to be associated with vertical fault at shallow depths.

The two LOS components from Sentinel-1 are not sensitive to N-S motion, so our profile analysis is based on the E-W component. We assumed the horizontal motion was mostly fault-parallel and assembled 3-km long, across-strike profiles within each 200-m window along-strike for each fracture. We then measured the amplitude and width of the deformation for each profile. The width data were corrected for the orientation of the fault relative to E-W. In total, we calculated 412 and 252 stacked profiles for prograde and retrograde fractures respectively. A number of profiles did not show significant deformation (e.g., when they are too close to the end of the fracture). Thus, we found 329 and 196 of them being applicable to the analysis, for prograde and retrograde respectively. The shear stress was then computed with the strike of these fractures being the receiver fault direction, and we used Eqn. (1) to calculate the corresponding shear modulus contrast. We tested both 10 GPa and 30 GPa when computing Coulomb stress and the shear modulus ratio, but found that this computed contrast does not yield a significant difference in the histogram distribution (Figure 2).

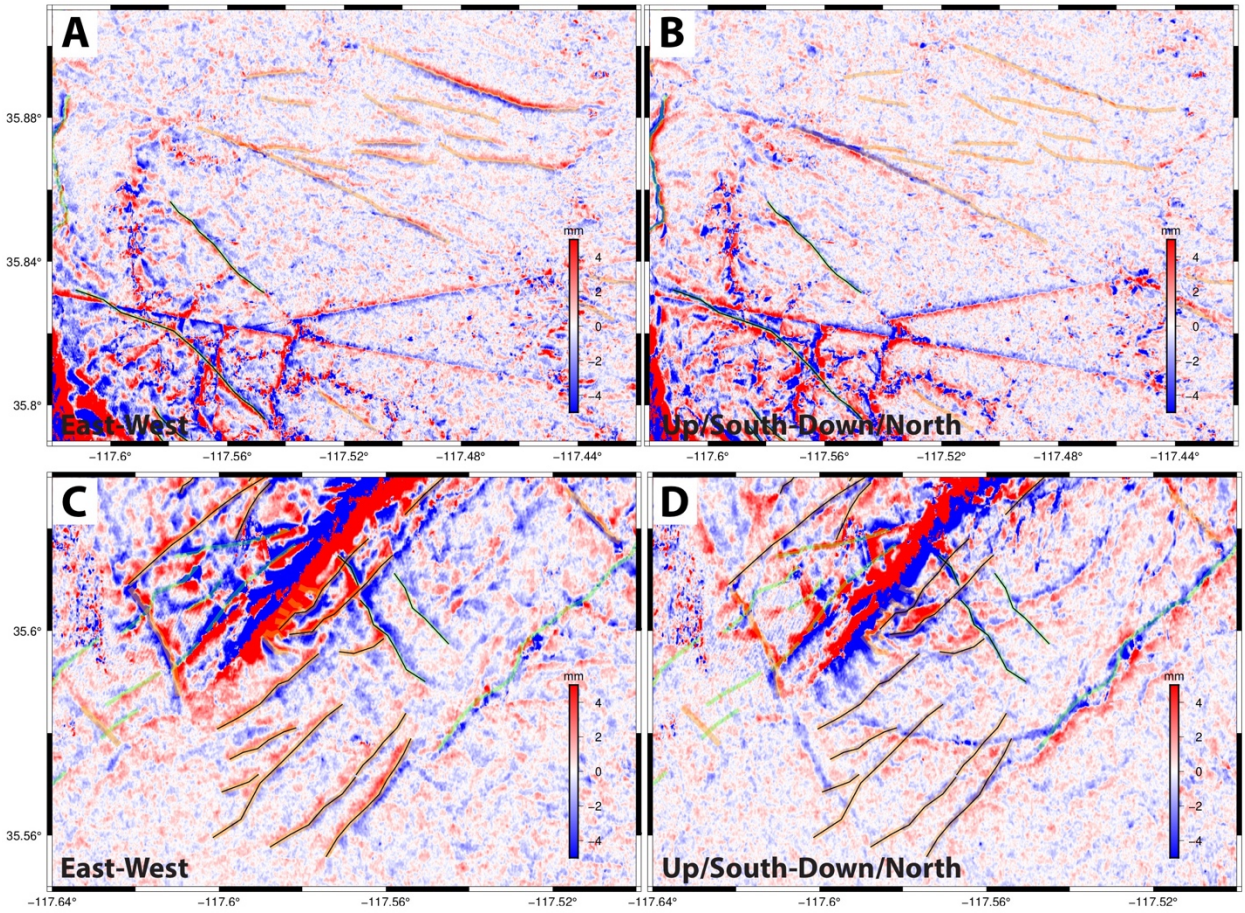

Fig. S1.
East-West and Up/South-Down/North displacement map for the boxed areas in Figure 1 (with marked deformation types). Right-lateral faults are marked by orange highlight and left-lateral faults are marked by green highlight. Black curves denote those that are identified as retrograde fractures. Note that most retrograde fractures have associated vertical motion along the fault, and they could be either left-lateral or right-lateral depending on the orientation.

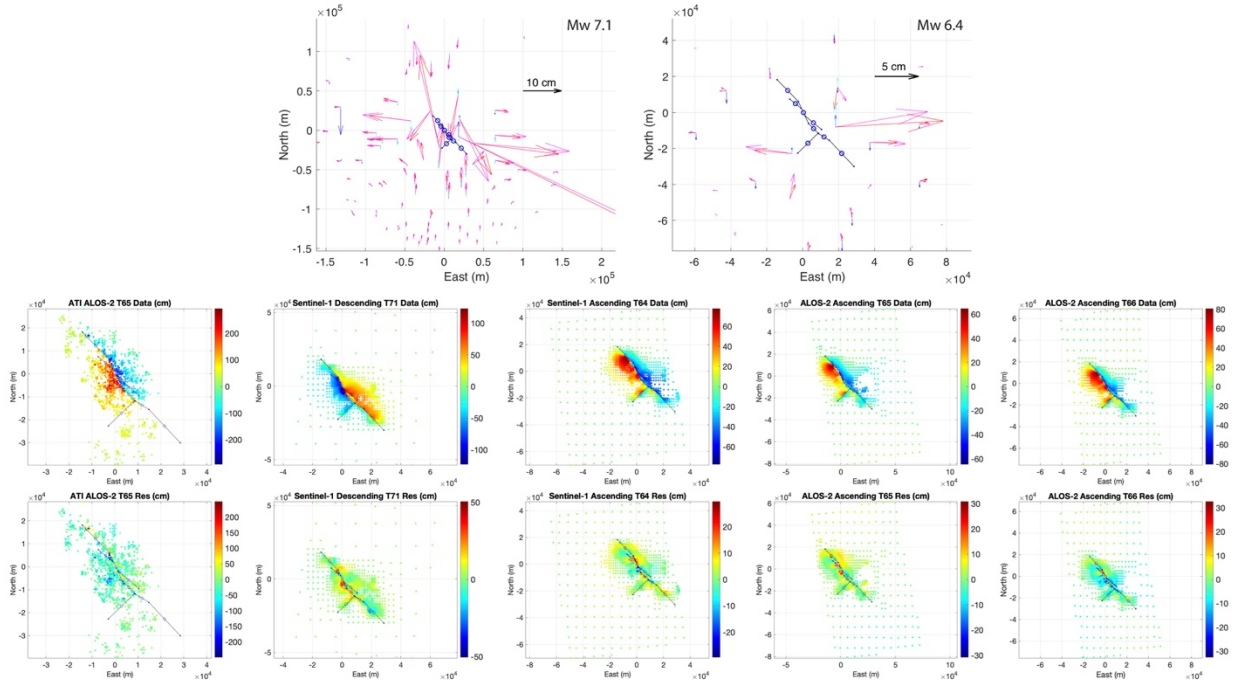

Fig. S2.
Slip inversion data and model fitting. Top panels are GNSS measurements and modeled offsets for each individual earthquake, with red and magenta arrows being observed and modeled horizontal displacements, blue and cyan arrows being observed and modeled vertical displacements. Bottom panels are quadtree subsampled InSAR data (top lane) and the slip model residues (bottom lane). Black segments are model fault planes with the blue circles denoting the center of each segment.

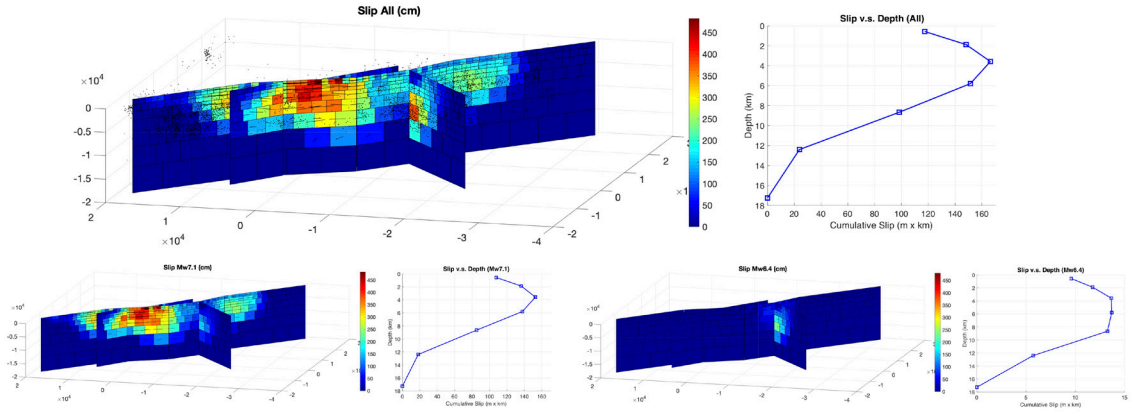

Fig. S3.
Slip source inversion results for the two events combined (top) and each individual event (bottom). The combined slip results are plotted with seismicity from Quick Template Matching (QTM) solutions (https://scedc.caltech.edu/research-tools/QTMcatalog.html).

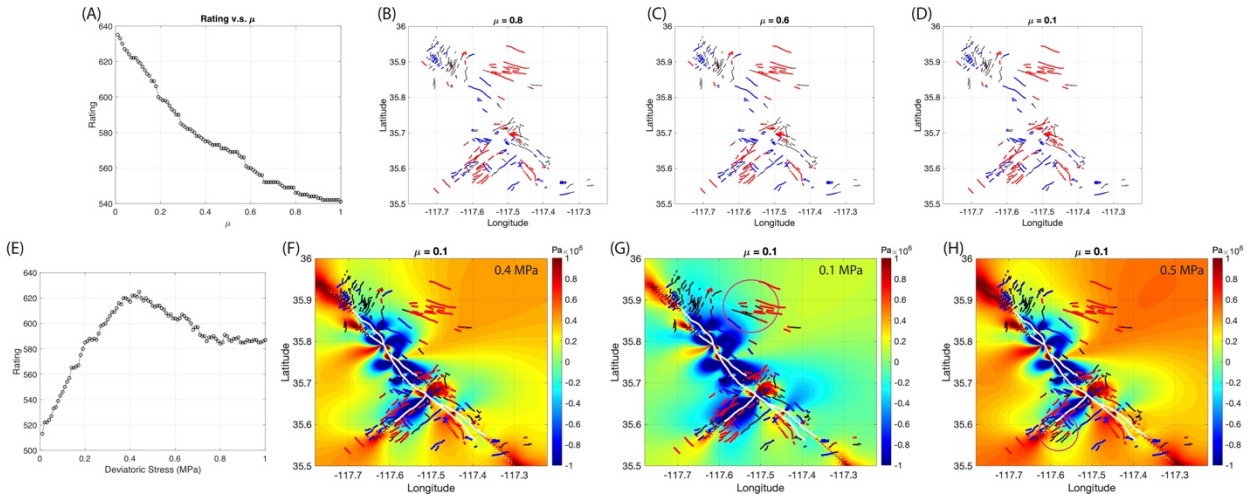

Fig. S4.

Stress change and frictional coefficient analysis. Inside each panel with faults, the red color lineaments denote fractures with observations that match predicted right-lateral motion from our Coulomb stress change analysis; the blue color lineaments denote fractures with observations that match predicted left-lateral motion from our Coulomb stress change analysis; black parts are those that failed to be predicted by Coulomb stress; white lines are fault rupture identified from phase gradient maps. The total number of segments analyzed here is 926 (note this includes part of the unidentified set of fractures). Panel (a) is the calculated number of matching segments (i.e. rating, total of red or blue) with respect to the frictional coefficient, μ_f. Panel (b), (c), and (d) are cases with fictional coefficient being 0.8, 0.6, and 0.1, respectively. Panel (e) is the calculated number of matching segments with respect to the added regional tectonic deviatoric stress. Panel (f), (g), and (h) are Coulomb stress change fields computed with low frictional coefficient 0.1 and receiver direction along the *Mw* 7.1 rupture, with added underlying deviatoric tectonic stress being 0.4 MPa, 0.1 MPa, and 0.5 MPa respectively. The red circle denotes places where the resulting stress change fields fail to predict the polarity. These analyses show that the shear stress plays a significant role in the polarity of these fractures, which are sensitive to an unknown additional deviatoric stress, for which we solve. In other words, it is the shear stress that determines the direction of the preferred slip, and normal stress combined with the frictional coefficient, serves as a "gate" that allows or prohibits slip from occurring.

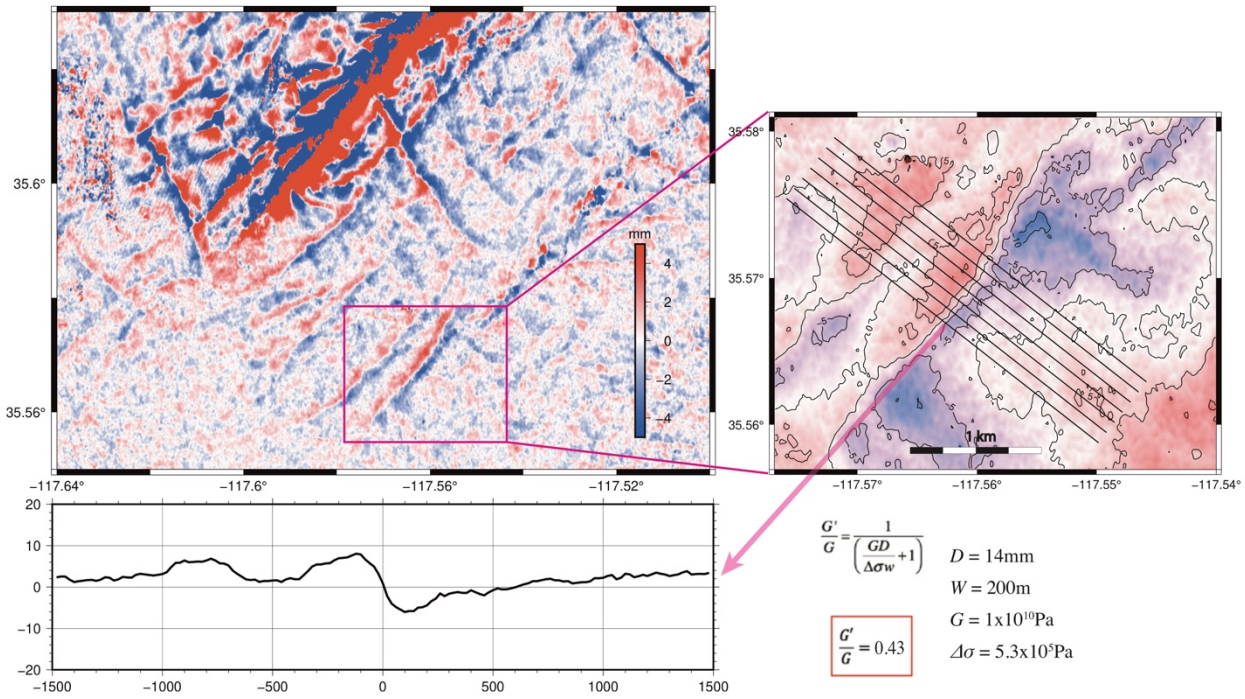

Fig. S5.
Displacement profile analysis. This analysis is performed on all of the fractures with the overall results displayed in Figure 2. The profiles are taken along each identified fracture with 200-m spacing within which data are averaged to provide a robust result. For more details, see the Coulomb stress, polarity matching and profile analysis section of the Materials and Methods.

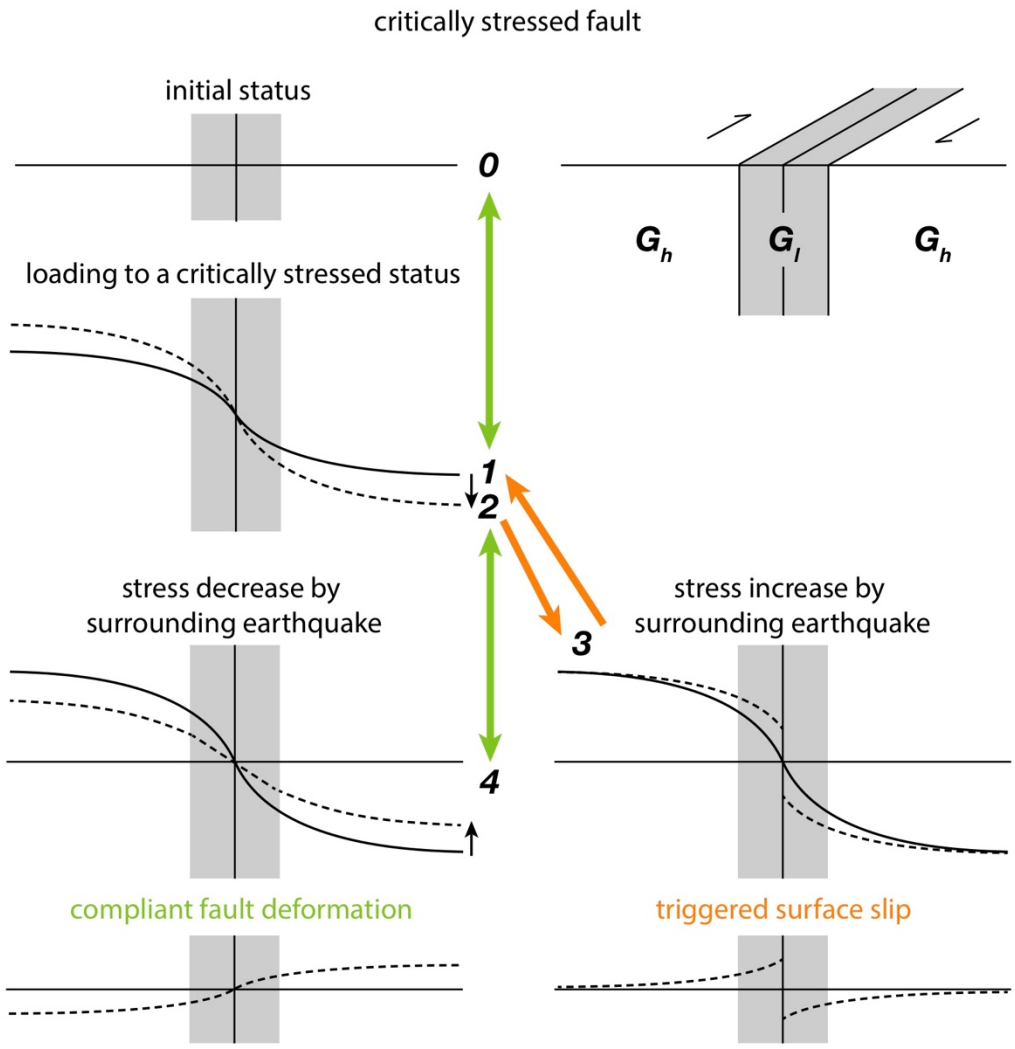

Fig. S6.
A more complete view of the conceptual model on explaining fracturing features. The initial status is an assumed start of the process, e.g. after an earthquake or a strong triggered event. With tectonic loading, the fault will slowly evolve into this critically stressed status, where a shallow fault will progress from 0 to 1 to 2 to 3 (frictional slip) and then back to 1. The fundamental assumption is that this deformation only partially releases the accumulated stress and the deformation status then returns to 1. Under this critically stressed status, the stress perturbation from a surrounding earthquake promotes prograde motion (3) and slip is more likely to arise as frictional slip model. When the stress perturbation promotes retrograde motion (4), due to the budget built from 0 to 1, the fault will likely remain within the elastic criteria, and behave as a compliant fault deformation. In the situation where a much stronger perturbation is involved, like remote triggering, either from a change in pore pressure or a drop of the frictional coefficient, stress changes may lead to a reset, consistent with the stress shadow effect observed on a number of faults (*31-32*). When there is an earthquake in the surrounding area, the results can be largely described as a two-scenario setup. When the resulting static stress increases, it's likely that the stress surpasses the threshold and leads to a frictional slip. When the resulting static stress decreases, due to the existence of a significant buffer built before the fault achieves a critically

stressed status, the deformation presumably will be compliant fault deformation. This buffer could possibly rely on the cohesion of the shallow fault material (*33*). The required stress change required to achieve a retrograde frictional slip is much larger than that needed to produce a prograde slip. Note that the stress change from a nearby earthquake will also change the critical stress criteria, and the threshold for frictional slip as well. This could explain certain cases where even the stress change promotes a retrograde slip, due to a strong decrease in normal stress that brings down the criteria to a much lower level, the resulting deformation continued as prograde motion, e.g., the faults to the southwest of Hector Mine earthquake (*10*). This model also explains the relatively small 0.4 MPa added tectonic deviatoric stress we estimate from ensuring the fracture motion transition. It is only the portion of stress that is beyond the critical stress status when added with the stress from the earthquakes and tectonic loading. Note that the critical stress criteria may have changed during the earthquake.

References and Notes

1. Z. E. Ross, B. Idini, Z. Jia, O. L. Stephenson, M. Zhong, X. Wang, Z. Zhan, M. Simons, E. J. Fielding, S.-H. Yun, E. Hauksson, A. W. Moore, Z. Liu, J. Jung, Hierarchical interlocked orthogonal faulting in the 2019 Ridgecrest earthquake sequence. *Science* **366**, 346–351 (2019). doi:10.1126/science.aaz0109 Medline

2. D. J. Ponti, J. L. Blair, C. M. Rosa, K. Thomas, A. J. Pickering, S. Akciz, S. Angster, J.-P. Avouac, J. Bachhuber, S. Bacon, N. Barth, S. Bennett, K. Blake, S. Bork, B. Brooks, T. Bullard, P. Burgess, C. Chupik, T. Dawson, M. DeFrisco, J. Delano, S. DeLong, J. Dolan, A. Donnellan, C. DuRoss, T. Ericksen, E. Frost, G. Funning, R. Gold, N. Graehl, C. Gutierrez, E. Haddon, A. Hatem, J. Helms, J. Hernandez, C. Hitchcock, P. Holland, K. Hudnut, K. Kendrick, R. Koehler, O. Kozaci, T. Ladinsky, R. Leeper, C. Madugo, M. Mareschal, J. McDonald, D. McPhillips, C. Milliner, D. Mongovin, A. Morelan, S. Nale, J. Nevitt, M. O'Neal, B. Olson, M. Oskin, S. Padilla, J. Patton, B. Philibosian, I. Pierce, C. Pridmore, N. Roth, D. Sandwell, K. Scharer, G. Seitz, D. Singleton, B. Smith-Konter, E. Spangler, B. Swanson, J. T. Jobe, J. Treiman, F. Valencia, J. Vanderwal, A. Williams, X. Xu, J. Zachariasen, J. Zimmerman, R. Zinke, Documentation of surface fault rupture and ground-deformation features produced by the 4 and 5 July 2019 M_w 6.4 and M_w 7.1 Ridgecrest earthquake sequence. *Seismol. Res. Lett.* **91**, 2942–2959 (2020). doi:10.1785/0220190322

3. P. L. Williams, S. F. McGill, K. E. Sieh, C. R. Allen, J. N. Louie, Triggered slip along the San Andreas fault after the 8 July 1986 North Palm Springs earthquake. *Bull. Seismol. Soc. Am.* **78**, 1112–1122 (1988).

4. P. Bodin, R. Bilham, J. Behr, J. Gomberg, K. W. Hudnut, Slip triggered on southern California faults by the 1992 Joshua Tree, Landers, and Big Bear earthquakes. *Bull. Seismol. Soc. Am.* **84**, 806–816 (1994).

5. M. J. Rymer, Triggered surface slips in the Coachella Valley area associated with the 1992 Joshua Tree and Landers, California, earthquakes. *Bull. Seismol. Soc. Am.* **90**, 832–848 (2000). doi:10.1785/0119980130

6. T. Wright, E. Fielding, B. Parsons, Triggered slip: Observations of the 17 August 1999 Izmit (Turkey) earthquake using radar interferometry. *Geophys. Res. Lett.* **28**, 1079–1082 (2001). doi:10.1029/2000GL011776

7. X. Xu, L. A. Ward, J. Jiang, B. Smith-Konter, E. Tymofyeyeva, E. O. Lindsey, A. G. Sylvester, D. T. Sandwell, Surface creep rate of the southern San Andreas fault modulated by stress perturbations from nearby large events. *Geophys. Res. Lett.* **45**, 10,259–10,268 (2018). doi:10.1029/2018GL080137

8. H. Goto, H. Tsutsumi, S. Toda, Y. Kumahara, Geomorphic features of surface ruptures associated with the 2016 Kumamoto earthquake in and around the downtown of Kumamoto City, and implications on triggered slip along active faults. *Earth Planets Space* **69**, 26 (2017). doi:10.1186/s40623-017-0603-9

9. D. T. Sandwell, L. Sichoix, D. Agnew, Y. Bock, J. B. Minster, Near real-time radar interferometry of the M_w 7.1 Hector Mine earthquake. *Geophys. Res. Lett.* **27**, 3101–3104 (2000). doi:10.1029/1999GL011209

10. Y. Fialko, D. Sandwell, D. Agnew, M. Simons, P. Shearer, B. Minster, Deformation on nearby faults induced by the 1999 Hector Mine earthquake. *Science* **297**, 1858–1862 (2002). doi:10.1126/science.1074671 Medline

11. Y. Fialko, Probing the mechanical properties of seismically active crust with space geodesy: Study of the coseismic deformation due to the 1992 M_w 7.3 Landers (southern California) earthquake. *J. Geophys. Res. Solid Earth* **109**, B03307 (2004). doi:10.1029/2003JB002756

12. A. A. Allam, Y. Ben-Zion, Seismic velocity structures in the Southern California plate-boundary environment from double-difference tomography. *Geophys. J. Int.* **190**, 1181–1196 (2012). doi:10.1111/j.1365-246X.2012.05544.x

13. X. Xu, D. T. Sandwell, B. Smith-Konter, Coseismic displacements and surface fractures from Sentinel-1 InSAR: 2019 Ridgecrest earthquakes. *Seismol. Res. Lett.* **91**, 1979–1985 (2020). doi:10.1785/0220190275

14. R. Torres, P. Snoeij, D. Geudtner, D. Bibby, M. Davidson, E. Attema, P. Potin, B. Ö. Rommen, N. Floury, M. Brown, I. N. Traver, P. Deghaye, B. Duesmann, B. Rosich, N. Miranda, C. Bruno, M. L'Abbate, R. Croci, A. Pietropaolo, M. Huchler, F. Rostan, GMES Sentinel-1 mission. *Remote Sens. Environ.* **120**, 9–24 (2012). doi:10.1016/j.rse.2011.05.028

15. A. Rosenqvist, M. Shimada, S. Suzuki, F. Ohgushi, T. Tadono, M. Watanabe, K. Tsuzuku, T. Watanabe, S. Kamijo, E. Aoki, Operational performance of the ALOS global systematic acquisition strategy and observation plans for ALOS-2 PALSAR-2. *Remote Sens. Environ.* **155**, 3–12 (2014). doi:10.1016/j.rse.2014.04.011

16. D. T. Sandwell, E. J. Price, Phase gradient approach to stacking interferograms. *J. Geophys. Res. Solid Earth* **103**, 30183–30204 (1998). doi:10.1029/1998JB900008

17. Materials and methods are available as supplementary materials.

18. J. Townend, M. D. Zoback, Regional tectonic stress near the San Andreas fault in central and southern California. *Geophys. Res. Lett.* **31**, L15S11 (2004). doi:10.1029/2003GL018918

19. X. Xu, X. Tong, D. T. Sandwell, C. W. D. Milliner, J. F. Dolan, J. Hollingsworth, S. Leprince, F. Ayoub, Refining the shallow slip deficit. *Geophys. J. Int.* **204**, 1867–1886 (2016). doi:10.1093/gji/ggv563

20. E. Klein, Y. Bock, X. Xu, D. T. Sandwell, D. Golriz, P. Fang, L. Su, Transient deformation in California from two decades of GPS displacements: Implications for a three-dimensional kinematic reference frame. *J. Geophys. Res. Solid Earth* **124**, 12189–12223 (2019). doi:10.1029/2018JB017201 Medline

21. C. Milliner, A. Donnellan, Using daily observations from Planet Labs satellite imagery to separate the surface deformation between the 4 July M_w 6.4 foreshock and 5 July M_w 7.1 mainshock during the 2019 Ridgecrest earthquake sequence. *Seismol. Res. Lett.* **91**, 1986–1997 (2020). doi:10.1785/0220190271

22. Y. Fialko, D. Sandwell, M. Simons, P. Rosen, Three-dimensional deformation caused by the Bam, Iran, earthquake and the origin of shallow slip deficit. *Nature* **435**, 295–299 (2005). doi:10.1038/nature03425 Medline

23. Y. Okada, Internal deformation due to shear and tensile faults in a half-space. *Bull. Seismol. Soc. Am.* **82**, 1018–1040 (1992).

24. P. Segall, *Earthquake and Volcano Deformation* (Princeton Univ. Press, 2010).

25. E. S. Cochran, Y. G. Li, P. M. Shearer, S. Barbot, Y. Fialko, J. E. Vidale, Seismic and geodetic evidence for extensive, long-lived fault damage zones. *Geology* **37**, 315–318 (2009). doi:10.1130/G25306A.1

26. J. F. Dolan, B. D. Haravitch, How well do surface slip measurements track slip at depth in large strike-slip earthquakes? The importance of fault structural maturity in controlling on-fault slip versus off-fault surface deformation. *Earth Planet. Sci. Lett.* **388**, 38–47 (2014). doi:10.1016/j.epsl.2013.11.043

27. H. M. Savage, E. E. Brodsky, Collateral damage: Evolution with displacement of fracture distribution and secondary fault strands in fault damage zones. *J. Geophys. Res. Solid Earth* **116**, B03405 (2011). doi:10.1029/2010JB007665

28. M. Oskin, L. Perg, D. Blumentritt, S. Mukhopadhyay, A. Iriondo, Slip rate of the Calico fault: Implications for geologic versus geodetic rate discrepancy in the Eastern California Shear Zone. *J. Geophys. Res. Solid Earth* **112**, B03402 (2007). doi:10.1029/2006JB004451

29. C. W. Chen, H. A. Zebker, Phase unwrapping for large SAR interferograms: Statistical segmentation and generalized network models. *IEEE Trans. Geosci. Remote Sens.* **40**, 1709–1719 (2002). doi:10.1109/TGRS.2002.802453

30. D. E. Goldberg, D. Melgar, V. J. Sahakian, A. M. Thomas, X. Xu, B. W. Crowell, J. Geng, Complex rupture of an immature fault zone: A simultaneous kinematic model of the 2019 Ridgecrest, CA earthquakes. *Geophys. Res. Lett.* **47**, e2019GL086382 (2020).

31. J. J. Lienkaemper, J. S. Galehouse, R. W. Simpson, Creep response of the Hayward fault to stress changes caused by the Loma Prieta earthquake. *Science* **276**, 2014–2016 (1997). doi:10.1126/science.276.5321.2014

32. E. Tymofyeyeva, Y. Fialko, J. Jiang, X. Xu, D. Sandwell, R. Bilham, T. K. Rockwell, C. Blanton, F. Burkett, A. Gontz, S. Moafipoor, Slow slip event on the southern San Andreas fault triggered by the 2017 M_w 8.2 Chiapas (Mexico) earthquake. *J. Geophys. Res. Solid Earth* **124**, 9956–9975 (2019). doi:10.1029/2018JB016765

33. J. Weiss, V. Pellissier, D. Marsan, L. Arnaud, F. Renard, Cohesion versus friction in controlling the long-term strength of a self-healing experimental fault. *J. Geophys. Res. Solid Earth* **121**, 8523–8547 (2016). doi:10.1002/2016JB013110